

# Single Shot Fluorescence Lifetime Imaging of Hydroxyl Radical Distributions and 3D Tomographic Reconstruction of Gliding Arc Discharge

S. Nilsson<sup>1</sup>, D. Sanned<sup>1</sup>, A. Roth<sup>1</sup>, M. Richter<sup>1</sup>, E. Berrocal<sup>1</sup> and A. Ehn<sup>1</sup>

<sup>1</sup> Division of Combustion Physics, Department of Physics, Lund University, Lund, Sweden

**Abstract:** Plasma discharges are complex 3D structures that can occur in various modes depending on various properties, such as pressure, current etc. We here present methods for instantaneous and simultaneous fluorescence lifetime imaging of hydroxyl radicals and 3D tomography that enables qualitative OH species distributions as well as detailed geometrical information of the plasma and its surrounding gas.

**Keywords:** gliding arc discharge, fluorescence lifetime imaging, 3D Tomography

## 1. Introduction

Many studies have been conducted on generating and diagnosing low-temperature plasma at atmospheric pressure. The gliding arc discharge is a typical low-temperature plasma that can be used in various applications such as combustion control, chemical reformation, and surface treatment [1]–[4]. Quantitative data are needed to obtain accurate understanding of the plasma discharge and its chemical impact. Laser-induced fluorescence is commonly used to study molecules and atoms and is particularly useful in plasma diagnostics because it is non-intrusive and species specific. However, quantitative measurements are sensitive to molecular collisions, which yields nonradiative losses and erroneous results. This work presents simultaneous instantaneous determination of OH fluorescence lifetimes and 3D rendering of the gliding arc discharge using Dual Imaging Modelling Evaluation (DIME) and 3D tomographic reconstruction. This combination of tools allows for studies of OH quenching and the geometric analysis of the discharge in different conditions and with different high voltage settings.

## 2. Methods

Fluorescence lifetime imaging algorithms typically utilize two Planar Laser Induced Fluorescence (PLIF) images where each pixel in the images corresponds to the same point in the image plane. Each image is acquired with different gate characteristics that capture different parts of the fluorescence lifetime decay curve. The two gate functions that are used in this study are displayed in Fig. 1 (a), where the  $G_{Long}$  captures the entire signal and  $G_{Short}$  captures the early part of the signal, which yields the images  $I_{Long}$  and  $I_{Short}$ , respectively. A ratio image can be formed between these images where the ratio value depends on the fluorescence decay time. When performing FLI with (DIME), this ratio image,  $D(x, y)$ , is formed between  $I_{Short}(x, y)$  and the sum of  $I_{Short}(x, y)$  and  $I_{Long}(x, y)$ :

$$D = \frac{I_{Short}}{I_{Short} + I_{Long}}. \quad (1)$$

To map an experimental ratio image,  $D$ , to fluorescence lifetimes, a detection system model is created using the known time gate functions  $G_j(t)$  and a library of temporally decaying signal  $S(t)$ . The detected intensity,

by each camera, can therefore be simulated using the following:

$$I_j = \int G_j(t)S(t). \quad (2)$$

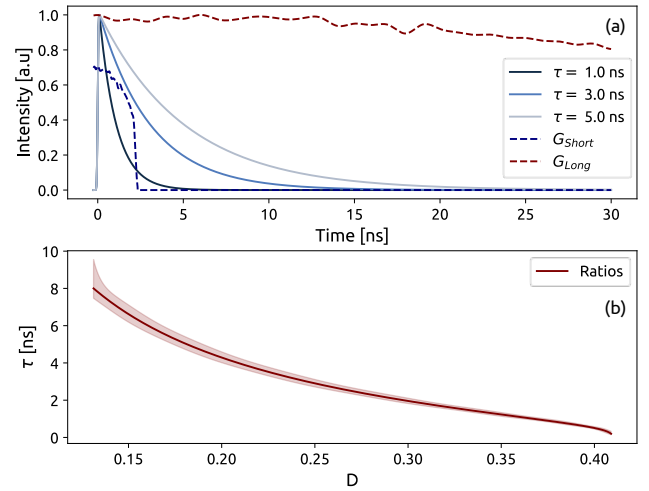


Figure 1: Simulated data which forms the model for the DIME method. (a) shows mono-exponential decay curves together with the gate functions for the long and short gates. (b) is the model of the simulated data using Equations (1) and (2) to map an intensity ratio to a lifetime. The shaded red area is the  $2\sigma$  uncertainty in the lifetime due to the jitter between the laser and cameras.

In this investigation,  $S(t)$  is a mono-exponential function with gate functions, with the index  $j$  denoting the long or the short camera gate. Simulating the relative detected intensities for a range of fluorescence lifetimes using Equations (2) and (3) generates a function that can correlate a ratio to a unique lifetime. This function, displayed in Fig. 2 (b), can convert a ratio  $D$  to a lifetime image  $\tau$ . A more detailed description and experimental considerations can be found in [5].

The 3D tomographic reconstruction was carried out using an in-house developed code which is based on the radiative transfer equation:

$$b_{qp} = \int_{qp} f(\vec{s}) dA \quad (3)$$

where  $f(\vec{s})$  is the continuous arc field and  $b_{qp}$  is the projection onto a camera view  $q$  and pixel  $p$ . Furthermore, to minimize the effects of noise and spurious scattering, a smoothness factor is introduced:

$$S = \iint (\Delta f(\vec{s}))^2 d\vec{s}. \quad (4)$$

Minimising Equation (4) results in a more continuous solution which is physically expected. Using Equations (3) and (4) allows the final reconstruction problem to be stated as follows:

$$f(\vec{s}) \min \sum_{qp} (b_{qp} - \int f(\vec{s}) dA) + \lambda S \quad (5)$$

where  $\lambda$  is the penalty term's weight, the minimization finds the reconstruction that best balances observational measurements against the applied smoothness requirement. A detailed description of the computational part and experimental considerations can be found in [6].

### 3. Experimental Setup

A gliding arc discharge system was studied under ambient conditions. The system includes three primary components: the electrodes, airflow, and power supply. The electrodes were made of stainless steel and were fixed to a Teflon plate. One of the electrodes was connected to a high-voltage power supply, and the other electrode served as ground. The airflow from a compressor was supplied through a 3 mm diameter hole in the Teflon plate between the two electrodes. The flow rates in the present experiment were controlled by a mass flow controller and are listed in Table 1, together with an estimation of their corresponding Reynolds numbers. The power of the discharge system was provided by a high-voltage alternating current (AC) power supply (Softal Electronic GmbH 6030). The AC power supply was operated at 35 kHz and delivered an input power between  $\sim 200$  W and  $\sim 1000$  W, depending on the flow rate. The AC power supply was operated at 5 Hz bursts with a 50 % duty cycle to ensure reproducible arc properties.

A 90 ps OPO (Ekspla FFL02) with a repetition rate of 5 Hz was set to 283 nm with a pulse energy of 1.6 mJ to excite the ground state OH, emitting fluorescence at 308 nm. The laser was formed into a sheet using a telescope and two cylindrical lenses with a height of approximately 30 mm. The emission from laser-excited OH\* was detected by two Andor iStar IsCMOS devices equipped with a Gen 2 image intensifier in a stereoscopic configuration. Both IsCMOS cameras were equipped with a Bernard Halle UV objective ( $f = 100$  mm,  $f/2$ ) and 32 mm extension rings to which Semrock 320/40 nm bandpass filters were attached. The camera gates for the  $G_{Long}$  and  $G_{Short}$  were set to 4 ns and 60 ns, respectively, to obtain good dynamics for the FLI measurements and suppress the plasma emission. Before data collection, the cameras were calibrated using a checkerboard target to ensure pixel overlap.

The 3D tomographic reconstruction was conducted using 10 Basler acA1920-40 gm cameras with a monochrome

Sony IMX249LLJ-C sensor and a Nikon objective ( $f = 28$  mm,  $f/4$ ) to capture the optical emission of the arc. The exposure time was set to 100  $\mu$ s to obtain a sufficient signal strength and temporarily freeze the arc.

The two IsCMOS cameras and tomographic cameras were triggered by a BNC Model 745T. The jitter between the IsCMOS cameras and the laser pulse was measured to have a standard deviation of 60 ps. The tomographic camera gate was centered around the laser pulse.

Table 1. Overview of the different flow conditions and their corresponding Reynolds number.

Flow Condition	Flow Rate	Reynolds Number
Low	4 l/min	1800
Medium	10 l/min	4000
High	20 l/min	9000

### 4. Results and Discussion

The fluorescence images captured when the gliding arc was operated with medium flow rate are shown in Fig. 2. The excitation laser cuts the plasma arc at the top of the arc perpendicular to the camera view, which generates a 'circular' shape with a hole in the center, as shown in the fluorescence images in Fig. 2 (a) and (b). The hole is the conduction channel of the plasma which OH surrounds. In (c) and (d), the ratio and lifetime image display the spatially varying lifetimes of the OH signal, respectively. The fluorescence lifetime image display some spatial variations in the OH-distribution but no drastic changes are seen. The plasma discharge does not, however, display any rapid mode transitions at this flowrate but instead show a rather diffuse emission around the gliding arc. Further investigations will be carried out at various operating conditions to study how fluorescence lifetimes are affected by flowrate and input power as well as geometrical aspects.

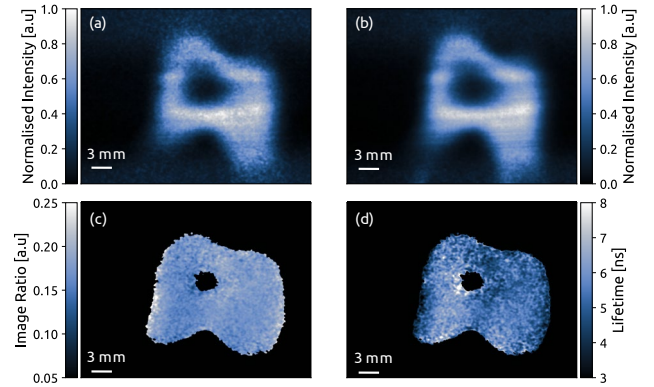


Figure 2: Example OH fluorescence images using the short and long gates in (a) and (b), respectively. In (c), the ratio between (a) and (b) is shown, forming the ratio image D. Lastly, in (d), the OH fluorescence lifetime image is displayed.

In Fig. 3, an example of the tomographic reconstruction of the optical emission from the high-flow case is displayed

from two angles: (a) and (b). The reconstructed volume was approximately  $90 \times 65 \times 60 \text{ mm}^3$ , which is sufficiently large to capture the entire structure of the arc discharge. It can be seen here that the arc itself is inherently a complex three-dimensional object, which would make it difficult to estimate the path length from a two-dimensional image.

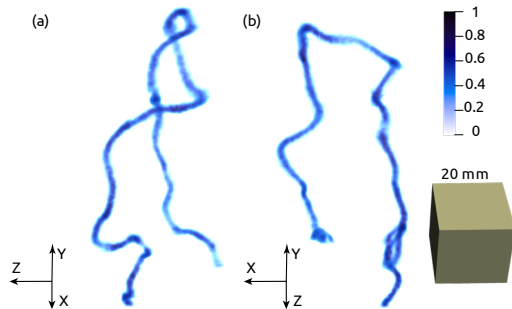


Figure 3: Example tomographic reconstruction of a gliding arc with normalized intensity in the high flow case. Where (a) and (b) displays two different view angles.

The path length and swept angle were calculated using a pathfinding algorithm to find the shortest path with the highest intensity between the two electrodes in 3D space. The swept angle measures the geometrical complexity of the arc and denotes the total change in angle from the anode to the cathode. The simplest shape is a semicircle with a total swept angle of  $\pi$  radians, similar to that shown in Fig. 4 in the low-flow example. Higher flow rates increase the complexity of the geometrical shape and, hence, the total swept angle, as shown in Fig. 5. There is a clear correlation between the arc length, swept angle, and deposited power for different flow rates. As the flow rate increased, the arc length increased, directly correlated to the swept angle, as indicated in Figs. 4 and 5.

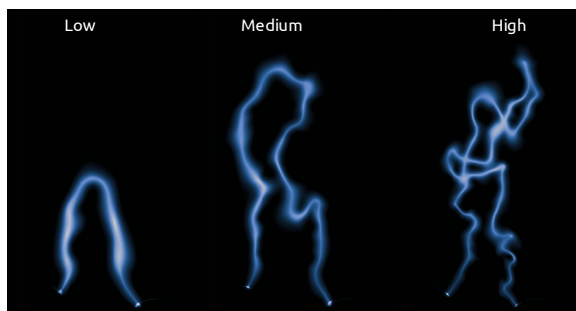


Figure 4: Example images from one of the tomography cameras displaying the complexity of the arc depending on the flow conditions.

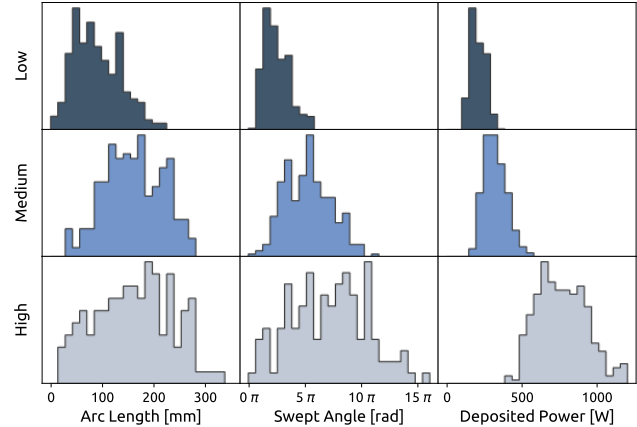


Figure 5: Extracted arc properties from 250 tomographic reconstructions for each flow rate with the average deposited power during each captured arc.

## 5. Summary

We present two diagnostic methods that are applied to characterize plasma properties in a gliding arc in terms of arc length, arc complexity, and fluorescence lifetimes. The fluorescence from  $\text{OH}^*$  was captured using two sCMOS cameras, and the fluorescence lifetime was determined using the DIME method. The results suggest that the lifetime around the conduction channel show some spatial variations but further investigations are needed to understand how laser-induced OH signals can be compared in different measurement conditions. The 3D tomography of the gliding arcs allows for accurate arc length determinations and provides insight into the geometrical complexity that cannot be obtained from a 2D image.

## 6. References

- [1] S. Y. Moon, W. Choe, and B. K. Kang, "A uniform glow discharge plasma source at atmospheric pressure," *Appl Phys Lett*, vol. 84, no. 2, pp. 188–190, Jan. 2004, doi: 10.1063/1.1639135.
- [2] Z. Feng, N. Saeki, T. Kuroki, M. Tahara, and M. Okubo, "Surface modification by nonthermal plasma induced by using magnetic-field-assisted gliding arc discharge," *Appl Phys Lett*, vol. 101, no. 4, Jul. 2012, doi: 10.1063/1.4738766.
- [3] L. L. Li *et al.*, "Magnetically enhanced gliding arc discharge for  $\text{CO}_2$  activation," *Journal of CO2 Utilization*, vol. 35, pp. 28–37, Jan. 2020, doi: 10.1016/J.JCOU.2019.08.021.
- [4] W. Z. Wang, M. Jia, R. Feng, and J. J. Zhu, "Experimental investigation on the gliding arc plasma supported combustion in the scramjet

combustor," *Acta Astronaut*, vol. 177, pp. 133–141, Dec. 2020, doi: 10.1016/J.ACTAASTRO.2020.07.027.

- [5] A. Ehn, O. Johansson, A. Arvidsson, M. Aldén, and J. Bood, "Single-laser shot fluorescence lifetime imaging on the nanosecond timescale using a Dual Image and Modeling Evaluation algorithm," *Opt Express*, vol. 20, no. 3, 2012, doi: 10.1364/oe.20.003043.
- [6] D. Sanned, J. Lindström, A. Roth, M. Aldén, and M. Richter, "Arbitrary position 3D tomography for practical application in combustion diagnostics," *Meas Sci Technol*, vol. 33, no. 12, 2022, doi: 10.1088/1361-6501/ac92a1.